NANO LETTERS

pubs.acs.org/NanoLett

Gate-defined graphene double quantum dot and excited state spectroscopy

Xing Lan Liu,* Dorothee Hug, and Lieven M. K. Vandersypen

Kavli Institute of Nanoscience, Delft University of Technology, P.O. Box 5046, 2600 GA Delft, The Netherlands

ABSTRACT A double quantum dot is formed in a graphene nanoribbon device using three top gates. These gates independently change the number of electrons on each dot and tune the interdot coupling. Transport through excited states is observed in the weakly coupled double dot regime. We extract from the measurements all relevant capacitances of the double dot system, as well as the quantized level spacing.

KEYWORDS Double quantum dot, graphene, excited state, top gate, disorder

Extensive efforts are made in investigating double quantum dots defined by electrostatic gates in various systems such as a GaAs two-dimensional electron gas,[1,2] semiconductor nanowires,[3] and carbon nanotubes,[4−7] with the motivation of realizing quantum computation schemes based on spins in quantum dots.[8] Graphene is a promising candidate for such applications due to the expected long spin coherence time[9,10] and flexibility in device designs offered by its two-dimensional nature. Accidental double dots formed by disorder were found in graphene nanoribbons.[11] More recently, graphene double dot devices have been realized by etching graphene into two small islands separated by a narrow constriction, where the interdot coupling was shown to be tunable by a side gate.[12,13] However, the tunability was limited partially due to the permanent presence of the constriction.

Here we define a double quantum dot device based on a graphene nanoribbon (GNR) using only local top gates. The device contains three top gates. The rightmost and leftmost top gate control the electron number on the right and left dot, respectively. A middle gate is used to tune the interdot coupling. The measurements exhibit familiar double dot characteristics.[1] In addition, when the interdot coupling is switched off by the middle gate, we observe excited states of the graphene double dot, which has not been reported before.[23] The design principle used here can be applied for defining single and multiple quantum dots along a GNR with independent gate control over barriers and charges.

The device is fabricated on graphene flakes deposited on a substrate by mechanical exfoliation of natural graphite.[14] The substrate consists of highly p-doped Si, covered with 285 nm thermally grown silicon dioxide. From their optical contrast against the substrate, we conclude that the flakes are single-layer.[15,16] Three electron beam lithography steps are used for fabricating the devices using PMMA as resist. First the source and drain electrodes are fabricated on selected graphene flakes. We use 5/50 nm thick e-beam evaporated Cr/Au as electrodes. In a second step, we cover the region where the GNR will be with 15 nm thick silicon dioxide using e-beam evaporation followed by lift-off. This SiO_2 layer not only acts as the etching mask for the GNR, but also forms part of the dielectric for the top gates. The GNR is then patterned by exposing it to an O_2/Ar (1:9) plasma[17] for 15 s. Without removing the SiO_2 etching mask, three local top gates, G1, G2, and G3 are fabricated in the last step. The gates consist of 5/5/20 nm thick e-beam evaporated SiO_2/Ti/Au, where an extra layer of SiO_2 is evaporated to ensure reliable top gate operations. Here we present measurements from a device where the GNR is 800 nm long and 20 nm wide. For this device, the middle gate G2 is 40 nm in width, separated by 80 nm from gate G1 and G3 which are both 600 nm wide. Figure 1 shows a scanning electron microscope image of a device of the same layout but smaller dimensions.

All measurements are performed in a dilution refrigerator at a base temperature of 50 mK. The electron temperature is around 150 mK. We measure the two-terminal resistance through the top gated GNR devices by applying a DC voltage

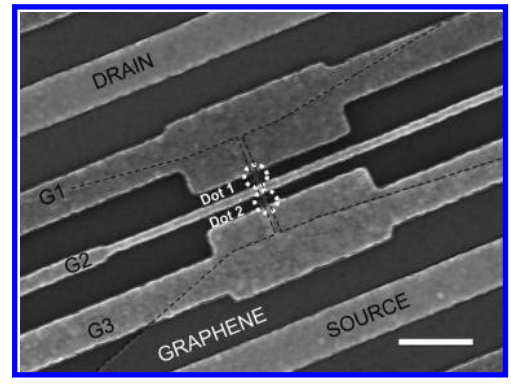

FIGURE 1. Scanning electron microscope image of a device similar to but smaller than the one that is measured in this work (scale bar 400 nm). The dashed lines outline the graphene nanoribbon and the dotted lines indicate dot 1 and dot 2.

* To whom correspondence should be addressed. E-mail: xinglan.liu@tudelft.nl.

Received for review: 12/10/2009
Published on Web: 04/08/2010

© 2010 American Chemical Society

DOI: 10.1021/nl9040912 | *Nano Lett.* **2010,** *10,* 1623–1627

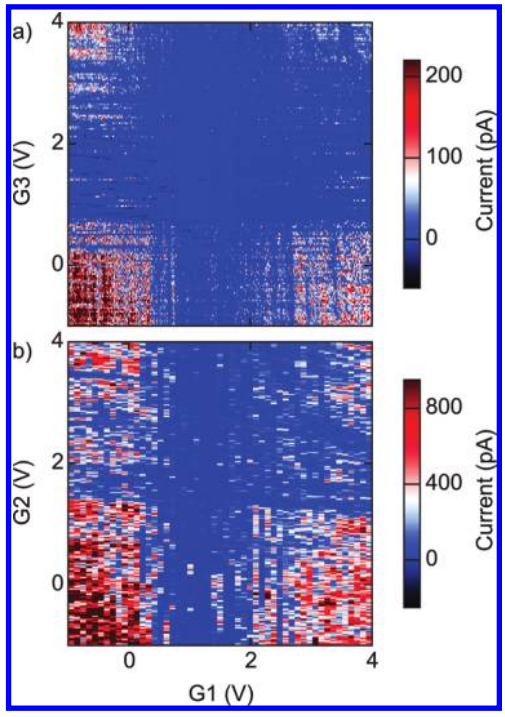

FIGURE 2. Device characterizations (a) Current as a function of top gate voltages V_{G1} and V_{G3} at $V_{G2} = 0$ and $V_{bias} = 100\ \mu V$. (b) Current as a function of top gate voltages V_{G1} and V_{G2} at $V_{G3} = 0$, and $V_{bias} = 300\ \mu V$.

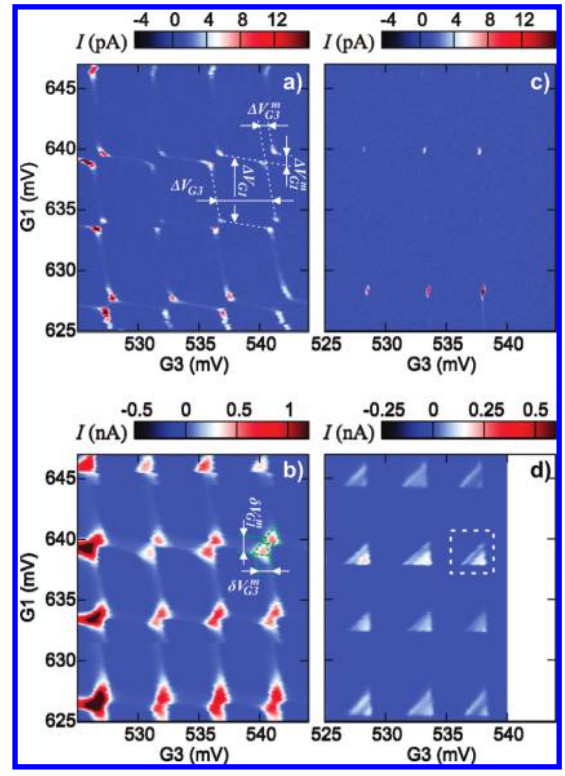

FIGURE 3. Current as a function of top gate voltages V_{G1} and V_{G3} (charge stability diagrams) in the double dot regime at (a) $V_{G2} = 1363$ mV and $V_{bias} = -15\ \mu V$; (b) $V_{G2} = 1363$ mV and $V_{bias} = 0.7$ mV; (c) $V_{G2} = 1380$ mV and $V_{bias} = -20\ \mu V$; (d) $V_{G2} = 1380$ mV and $V_{bias} = 1.35$ mV. Color scales represent the absolute value of current through the double dot. The white (a) and green (b) dotted lines are guides to the eye showing the honeycomb patterns and the bias triangles. The relevant parameters are also illustrated in (a) and (b). The dashed line in (d) encloses the triple points where the measurements in Figure 4a,b and 5 are taken. The two horizontal shifts at $V_{G1} = 644.5$ mV and 631.4 mV in (b) are due to charge switching events.

bias on the source electrode and measuring the current at the drain electrode. The degenerately doped Si substrate is grounded.

The GNR is intrinsically hole-doped when all gates are at zero voltage. Figure 2a shows the low bias conductance as a function of G1 and G3 while G2 is fixed at zero voltage. When either of the gate voltages is above 0.5 V, current is suppressed by 3−4 orders of magnitude, as the Fermi level enters the transport gap locally under the top gates. The conductance increases again when the voltage on either gate is increased further to above 3 V, where the Fermi level is locally in the conduction band and the electrons that are induced in the GNR contribute to transport. The pinch-off voltage for one gate is nearly independent of the other, indicating little cross-coupling in this configuration. Similarly, Figure 2b shows the low bias conductance as a function of gate G1 and G2 while G3 is fixed at zero voltage. Current is also suppressed by 3 to 4 orders of magnitude when the applied voltage on G2 is above 1.3 V. The pinch-off voltage of G2 is higher than that of G1 and G3, and shows a mild dependence on V_{G1}. The voltage on G2 is increased further up to 4 V, but the ribbon below G2 still does not reach heavily n-doping.

A double quantum dot is formed when the voltages on all three gates are increased to close to pinch-off. Figure 3a plots the low bias conductance as a function of the voltages on G1 and G3, measured at $V_{G2} = 1363$ mV. It shows a regular honeycomb pattern characteristic of the charge stability diagram of a double quantum dot.[1] The gates G1 and G3 control the number of holes on dot 1 and 2, respectively. Resonant transport occurs at the triple points. Due to cotunneling we also measure a finite current along all boundaries of the hexagons. From the size of the hexagons, the peak spacing in G1 and G3 is extracted to be $\Delta V_{G1} = 6$ mV and $\Delta V_{G3} = 5$ mV, respectively. Thus the capacitance from dot 1 to gate G1 is $C_{G1} \approx e/\Delta V_{G1} = 27$ aF, and that from dot 2 to gate G3 is $C_{G3} \approx e/\Delta V_{G3} = 32$ aF, assuming zero level spacing. The large capacitive coupling to these gates indicates that the dot extends far under the gates. Thus the barriers are likely to be induced by the disorder potential instead of being defined by electrostatic potentials induced by the top gates, similar to earlier work.[11,18,19] We estimate from the capacitance values that dot 1 (2) extends to roughly 160 nm under gate G1 (G3).[20] Since the spacing between G1 (G3) and G2 is 80 nm and the ribbon is 20 nm wide, we then assume that the area A of each dot is around 240 nm by 20 nm. The large capacitive coupling allows G1 and G3 to change the number of carriers on dot 1 and dot 2, respectively. Assuming that holes cross over to electrons at around $V_{G1,G3} \approx 1.3$ V, we roughly

© 2010 American Chemical Society

DOI: 10.1021/nl9040912 | Nano Lett. 2010, 10, 1623–1627

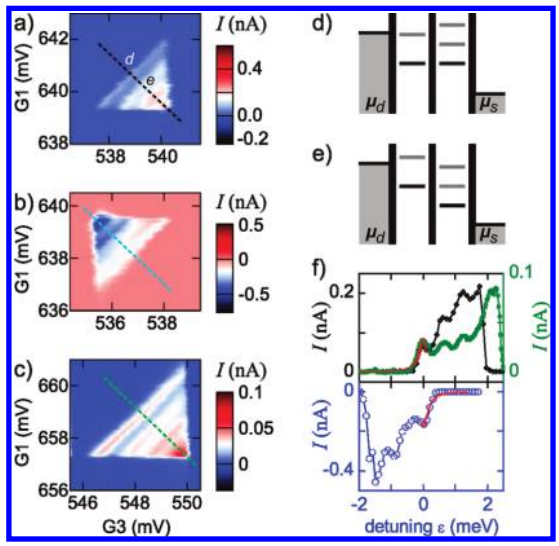

FIGURE 4. Resonant transport through excited states in the double dot. Current as a function of top gate voltages V_{G1} and V_{G3} at (a) V_{G2} = 1380 mV and V_{bias} = 1.9 mV; (b) V_{G2} = 1380 mV and V_{bias} = −1.9 mV; (c) V_{G2} = 1370 mV and V_{bias} = 2.8 mV. The dotted lines indicate the detuning axis. (d, e) Energy level schemes of the double dot corresponding to the points *d* and *e* in (a). Black solid lines represent the ground states and gray lines represent excited states. The chemical potentials of the source and drain contacts are denoted as μ_s and μ_d, respectively. (f) Line cuts along the detuning axis. The black diamonds, blue circles, and green squares are line-cuts from (a−c), respectively. The red solid lines are Lorentzian fits to the right edges of the ground state lines.

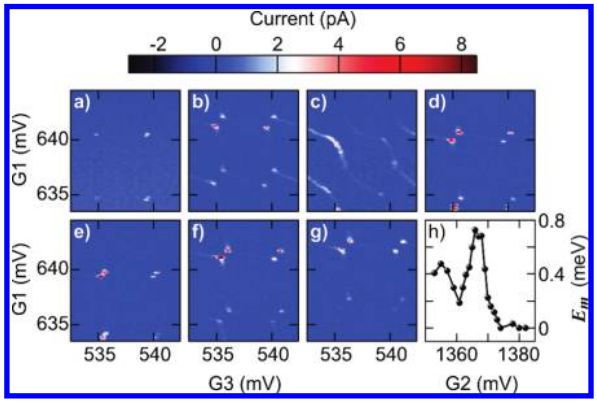

FIGURE 5. Interdot coupling vs middle gate voltage V_{G2}. Current as a function of top gate voltages V_{G1} and V_{G3} at V_{bias} = 15 μV and (a) V_{G2} = 1373 mV, (b) V_{G2} = 1369 mV, (c) V_{G2} = 1367 mV, (d) V_{G2} = 1363 mV, (e) V_{G2} = 1361 mV, (f) V_{G2} = 1359 mV, (g) V_{G2} = 1357 mV, measured at around the same charge configuration as that of Figure 4a. (h) The interdot coupling energy E_m as a function of V_{G2} extracted from (a−g) and similar measurements.

estimate that in the voltage configuration of Figure 3 each dot contains around 150 holes, giving a hole density $n = 3 \times 10^{12}$ cm^{-2}.

The splitting between each pairs of triple points is indicative of the coupling between the two dots. For the pair of triple points highlighted by the dashed lines in Figure 3a, the splitting is $\Delta V_{G1}^m = \Delta V_{G3}^m = 0.9$ mV. When the bias voltage is increased, each triple point grows into a triangle due to inelastic transport,[1] as shown in Figure 3b. From the size of the triangles, we extract conversion factors between gate voltages and energy to be $\alpha_1 = eV_{bias}/\delta V_{G1} \approx 0.4e$ and $\alpha_3 = eV_{bias}/\delta V_{G3} \approx 0.4e$. The charging energy of dot 1 and dot 2 is then $E_{c1} = e^2/C_1 = \alpha_1 e/C_{G1} \approx 2.6$ meV, and $E_{c2} = e^2/C_2 = \alpha_3 e/C_{G3} \approx 2.2$ meV, respectively, where C_1 and C_2 are the total capacitances of dot 1 and dot 2. Applying a model for purely capacitively coupled double dots,[1] we extract the interdot coupling capacitance $C_m = C_2 C_{G1} \Delta V_{G1}^m/e = C_1 C_{G3} \Delta V_{G3}^m/e \approx 11$ aF, and the coupling energy $E_m = e^2/C_m(C_1C_2/C_m^2 - 1)^{-1} = 0.4$ meV. Table 1 lists also other capacitance values estimated from the hexagons (level spacing is not taken into account in this case), where $C_{G1\text{-}2(G3\text{-}1)}$ is the cross capacitance between G1 (G3) and dot 2 (dot 1).

TABLE 1. Capacitance Values (in aF) Extracted from the Honeycomb Diagrams Shown in Figure 3

V_{G2} (mV)	C_{G1}	C_{G3}	C_1	C_2	$C_{G1\text{-}2}$	$C_{G3\text{-}1}$
1363	27	32	59	77	5	6
1380	28	38	44	59	0	0

A further change of the voltage on the gate G2 changes the interdot coupling. When V_{G2} = 1380 mV, the interdot coupling is practically zero, and the charge stability diagram consists of rectangular cells with overlapping triple points (Figure 3c). Figure 3d shows high-bias measurements in the same regime, where the pairs of triangles also overlap as a result of the small interdot coupling. Resonant transport through excited states is clearly visible in every triple point (the excited states are discussed further below). In this regime, we extract the energy conversion factors to gates G1 and G3 as $\alpha_1 = \alpha_3 \approx 0.6e$. The charging energies of the two dots are $E_{c1} = 3.6$ meV and $E_{c2} = 2.7$ meV, much larger than in the previous regime of strong interdot coupling. Other capacitance values estimated from the stability diagram are also listed in Table 1, where a level spacing value of 0.5 meV is included in the estimate for this G2 voltage value.

We now discuss in detail the excited-state patterns. Figure 4a and 4b show high resolution measurements of the pair of overlapping triple points enclosed by the dashed line in Figure 3d at different bias voltages. Along the baseline of the triangle the ground states of the two dots are aligned, and at the center of the baseline (point *d*), they lie exactly in the middle of the bias window, as illustrated by the level scheme in Figure 4d. At positive bias (Figure 4a), moving along a line from point *d* to the tip of the triangle (the detuning axis), the energy levels in dot 1 shift upward while those in dot 2 shift downward. At point *e*, the ground state of dot 1 aligns exactly with the first excited state of dot 2 (Figure 4e), and resonant transport occurs. The nonresonant background current level is caused by inelastic processes. From these data, the level spacing of dot 2 is extracted to be around 0.6 meV in this charge configuration. At large negative bias, resonant lines parallel to the baseline are also observed (Figure 4b) due to resonant transport through the ground state of dot 2 and excited states of dot 1. The level spacing

© 2010 American Chemical Society

DOI: 10.1021/nl9040912 | *Nano Lett.* **2010,** *10,* 1623–1627

of dot 1 is around 0.6 − 0.9 meV. The measured level spacing is comparable to the average level spacing estimated using $\delta E \approx 1/(D(E_F)A) \approx 0.7$ meV, where $D(E_F)$ is the density of states per unit area for 2D graphene at the Fermi energy and is calculated based on the hole density in the dot estimated earlier. For this triple point, the peak current levels of the excited state lines are slightly higher than that of the baseline, likely because the excited states are better coupled to the source/drain contacts.[1,7] In Figure 4c, we show another pair of overlapping triple points measured at a slightly different charge configuration, where the resonant current through the ground state and excited state are nearly equal.

Transport through the excited states can be analyzed more quantitatively using the result from Stoof and Nazarov for resonant tunneling.[1,21] In the limit of weak interdot tunnel coupling $t_m \ll \Gamma_{i,o}$, where t_m is the interdot tunnel coupling, and $\Gamma_{i,o}$ are incoming and outgoing tunnel rates, the current I follows a Lorentzian line shape as a function of detuning ε, $I(\varepsilon) = (4et_m^2/\Gamma_o)/(1 + (2\varepsilon/h\Gamma_o)^2)$, with h the Plank constant. Figure 4f plots line-cuts along the detuning axis for both positive and negative bias, and Lorentzian line fits to the ground state lines. The fitting is done for the data points outside of the bias triangle in order to minimize the contributions from the inelastic transport.[22] We extract from the fittings a tunnel rate from dot 1 to the drain $h\Gamma_1 \approx 350$ μeV, from dot 2 to the source $h\Gamma_3 \approx 280$ μeV, and an interdot tunnel rate $ht_m \approx 10$ μeV. We note that the ground state resonance lines overlap partially with the excited state lines because the tunnel rates to the leads are comparable to the level spacing. This overlap is not taken into account for the fit.

The interdot coupling changes nonmonotonously as a function of V_{G2}, similar to ref 12. Figure 5 shows additional data on the evolution of the pair of triple points in Figure 3a,b, as the voltage on G2 is changed in small steps. Clearly, the splitting between the triple points changes as V_{G2} is varied. This is also shown in Figure 5h where the interdot coupling energy E_m extracted from the data is plotted as a function of V_{G2}. The coupling energy can be tuned from around 0.7 meV down to virtually zero. However, the oscillating behavior suggests that most likely, the change of interdot coupling is partially due to resonances induced by disorder close to gate G2.

There is likely to be disorder close to gates G1 and G3 as well. This could be the reason for the observation that even when the voltage on G2 is fixed, the vertex splittings and the peak conductance of the vertices vary for different V_{G1} or V_{G3} (Figure 3 and Figure 5). It indicates that the gates G1 and G3 also change the dot-to-lead couplings in a similar nonmonotonous manner as G2, in addition to controlling the number of carriers on each dot. We also tried to form a single dot through the ribbon by lowering the voltage on the gate G2 to close to zero, but the device could not be tuned to a regime where a well-defined single dot is formed,[20] mainly due to strong disorder. At present, disorder thus substantially limits the control over our device. We note however that this is not intrinsic to the device design.

In conclusion, a double quantum dot device is realized in a graphene nanoribbon with multiple top gates. Resonant transport through excited states is observed. The interdot coupling strength is tunable over a wide range by the middle gate, although the coupling changes nonmonotonously with gate voltage as a result of disorder. Disorder poses a major challenge for future device applications in the field of quantum information processing and further progress is needed in order to suppress the influence of disorder on the tunability of the device. We also anticipate that adding two more gates to the left and right dots would allow one to control the number of charges on the two dots and the barriers to the leads separately, which would further improve the controllability of a graphene double dot device.

Acknowledgment. We thank Georg Goetz for useful discussions. This work is supported by the Dutch Foundation for Fundamental Research on Matter (FOM).

Supporting Information Available. Estimate of dot area and single dot data where disorder modifies the dot potential. This material is available free of charge via the Internet at http://pubs.acs.org.

REFERENCES AND NOTES

(1) van der Wiel, W. G.; De Franceschi, S.; Elzerman, J. M.; Fujisawa, T.; Tarucha, S.; Kouwenhoven, L. P. *Rev. Mod. Phys.* **2003**, *75* (1), 1.
(2) Hanson, R.; Kouwenhoven, L. P.; Petta, J. R.; Tarucha, S.; Vandersypen, L. M. K. *Rev. Mod. Phys.* **2007**, *79* (4), 1217.
(3) Fasth, C.; Fuhrer, A.; Bjork, M. T.; Samuelson, L. *Nano Lett.* **2005**, *5* (7), 1487–1490.
(4) Mason, N.; Biercuk, M. J.; Marcus, C. M. *Science* **2004**, *303* (5658), 655.
(5) Biercuk, M. J.; Garaj, S.; Mason, N.; Chow, J. M.; Marcus, C. M. *Nano Lett.* **2005**, *5* (7), 1267–1271.
(6) Graber, M. R.; Weiss, M.; Oberholzer, S.; Schonenberger, C. *Semicond. Sci. Technol.* **2006**, *21* (11), S64–S68.
(7) Sapmaz, S.; Meyer, C.; Beliczynski, P.; Jarillo - Herrero, P.; Kouwenhoven, L. P. *Nano Lett.* **2006**, *6* (7), 1350–1355.
(8) Loss, D.; DiVincenzo, D. P. *Phys. Rev. A* **1998**, *57* (1), 120.
(9) Trauzettel, B.; Bulaev, D. V.; Loss, D.; Burkard, G. *Nat. Phys.* **2007**, *3* (3), 192.
(10) Fischer, J.; Trauzettel, B.; Loss, D. *Phys. Rev. B* **2009**, *80* (15), 155401.
(11) Todd, K.; Chou, H.-T.; Amasha, S.; Goldhaber-Gordon, D. *Nano Lett.* **2009**, *9* (1), 416–421.
(12) Molitor, F.; Dröscher, S.; Güttinger, J.; Jacobsen, A.; Stampfer, C.; Ihn, T.; Ensslin, K. *Appl. Phys. Lett.* **2009**, *94* (22), 222107.
(13) Moriyama, S.; Tsuya, D.; Watanabe, E.; Uji, S.; Shimizu, M.; Mori, T.; Yamaguchi, T.; Ishibashi, K. *Nano Lett.* **2009**, *9* (8), 2891–2896.
(14) Novoselov, K. S.; Geim, A. K.; Morozov, S. V.; Jiang, D.; Zhang, Y.; Dubonos, S. V.; Grigorieva, I. V.; Firsov, A. A. *Science* **2004**, *306* (5696), 666.
(15) Blake, P.; Hill, E. W.; Castro Neto, A. H.; Novoselov, K. S.; Jiang, D.; Yang, R.; Booth, T. J.; Geim, A. K. *Appl. Phys. Lett.* **2007**, *91* (6), No. 063124.

© 2010 American Chemical Society

DOI: 10.1021/nl9040912 | *Nano Lett.* **2010,** *10,* 1623–1627

(16) Oostinga, J. B.; Heersche, H. B.; Liu, X.; Morpurgo, A. F.; Vandersypen, L. M. K. *Nat. Mat.* **2008**, *7* (2), 151–157.
(17) Stampfer, C.; Guettinger, J.; Molitor, F.; Graf, D.; Ihn, T.; Ensslin, K. *Appl. Phys. Lett.* **2008**, *92* (1), No. 012102.
(18) Stampfer, C.; Guettinger, J.; Hellmuller, S.; Molitor, F.; Ensslin, K.; Ihn, T. *Phys. Rev. Lett.* **2009**, *102* (5), No. 056403.
(19) Liu, X.; Oostinga, J. B.; Morpurgo, A. F.; Vandersypen, L. M. K. *Phys. Rev. B* **2009**, *80* (12), 121407.
(20) See the Supporting Information.
(21) Stoof, T. H.; Nazarov, Yu. V. *Phys. Rev. B* **1996**, *53* (3), 1050.
(22) Steele, G. A.; Goetz, G.; Kouwenhoven, L. P. *Nat. Nanotechnol.* **2009**, *4* (6), 363.
(23) The following work was performed simultaneously with ours. Molitor, F.; Knowles, H.; Dröscher, S.; Gasser, U.; Choi, T.; Roulleau, P.; Güttinger, J.; Jacobsen, A.; Stampfer, C.; Ensslin, K.; Ihn, T. arXiv: 1001.4700.

© 2010 American Chemical Society

DOI: 10.1021/nl9040912 | *Nano Lett.* **2010,** *10,* 1623–1627